

ABS: an Analytical method of Blind Separation of CMB from foregrounds

Pengjie Zhang^{1,2,3,4*}, Jun Zhang^{1,4}, Le Zhang^{1,4}

¹Department of Astronomy, School of Physics and Astronomy, Shanghai Jiao Tong University, 955 Jianchuan road, Shanghai, 200240

²IFSA Collaborative Innovation Center, Shanghai Jiao Tong University, Shanghai 200240, China

³Tsung-Dao Lee Institute, Shanghai 200240, China

⁴Shanghai Key Laboratory for Particle Physics and Cosmology

6 April 2019

ABSTRACT

Extracting CMB B-mode polarization from complicated foregrounds is a challenging task in searching for inflationary gravitational waves. We propose the ABS method as a blind and analytical solution to this problem. It applies to the measured cross bandpower between different frequency bands and obtains the CMB B-mode bandpower analytically. It does not rely on assumptions of foregrounds and does not require multiple parameter fitting. Testing against a variety of foregrounds, survey frequency configurations and instrument noise, we verify its applicability and numerical stability. The ABS method also applies to CMB temperature, E-mode polarization, the thermal Sunyaev Zel’dovich effect, spectral distortion, and even significantly different problems such as cosmic magnification.

Key words: Cosmology: inflation:cosmic microwave background

1 INTRODUCTION

Searching for inflationary gravitational waves (Starobinskiĭ 1979) through the induced CMB B-mode polarization (Seljak & Zaldarriaga 1997; Seljak 1997; Kamionkowski et al. 1997) is a major endeavour of cosmology (e.g. BICEP: BICEP2 Collaboration et al. (2014); Grayson et al. (2016); BICEP2/Keck and Planck Collaborations et al. (2015); ACTpol: Thornton et al. (2016); SPTpol: Keisler et al. (2015); POLARBEAR: Inoue et al. (2016); PIPER: Gandilo et al. (2016); CORE: Delabrouille et al. (2017); EPIC: Bock et al. (2008); LiteBIRD: Matsumura et al. (2014); PIXIE: Kogut et al. (2011); PRISM: André et al. (2014); AliCPT: Li et al. (2017)). It will open a window into the very beginning of our universe.

A major challenge of CMB B-mode detection is to accurately remove polarized galactic foregrounds (Planck Collaboration et al. 2015a,b,c). At CMB frequency of ~ 100 GHz, a major foreground is the galactic thermal dust, which likely dominates over CMB B-mode at $\nu \gtrsim 100$ GHz, even for the cleanest sky areas (BICEP2/Keck and Planck Collaborations et al. 2015). Synchrotron emission may be another major foreground, especially at lower frequency. Other polarized foregrounds such as spinning dust (Planck Collaboration et al.

2011, 2015a) and magnetic dust (Draine & Hensley 2012; Planck Collaboration et al. 2015d) may also be non-negligible.

Usually CMB experiments rely on multi-frequency information to remove foregrounds (e.g. Planck Collaboration et al. (2015a,b,c); Kogut et al. (2011); André et al. (2014)). This kind of approaches faces a major uncertainty, namely the exact frequency dependences of foregrounds and the exact number of independent foreground components are unknown. For example, recently Planck found that dust foregrounds at 217 and 353 GHz bands are decorrelated at a few percent level, meaning the existence of multiple dust components. This may lead to a significant bias in r (tensor-to-scalar ratio) (Remazeilles et al. 2016; Planck Collaboration et al. 2016a; Poh & Dodelson 2016). To avoid such potential bias, various methods blind of foregrounds, such as the internal linear combination (ILC) method and the independent component analysis (ICA) method, have been constructed (e.g. the review article by Delabrouille & Cardoso (2007)). Many of them have been applied in CMB observations such as WMAP and Planck, and enabled high precision CMB measurements (e.g. Planck Collaboration et al. (2015b, 2018) for a summary). Nevertheless, given the stringent requirement of accurate CMB measurement, there are still ongoing efforts to improve existing methods or developing new methods (e.g. Umiltà et al. (2018)). Here we report the **ABS** method, which stands for the **A**nalytical method

* E-mail: zhangpj@sjtu.edu.cn

of Blind Separation of CMB from foregrounds. It can be treated as post-processing on the matrix of cross bandpower between frequency bands, which are heavily compressed products of the original (noisy) maps. It works on any single multipole bin. Due to the fact that CMB B-mode has a known (blackbody) frequency dependence, a set of specific linear algebra operations on this measured matrix automatically returns the bandpower $\mathcal{D}_B(\ell)$, the most important B-mode statistics. The measurement procedure is completely fixed by the measured matrix and survey specifications, with no assumptions on foregrounds. Since it does not rely on fitting procedures, it is numerically stable and fast.

This paper is organized as follows. In §2 we describe the ABS method. In §3 we generate simulated data with various foreground components, CMB B-mode, survey frequency configurations and instrumental noise. In §4 we test the ABS method against these simulated data. In §5 we derive the necessary and sufficient survey conditions for unbiased CMB measurement. In §6 we briefly discuss and compare ABS with the ILC and SMICA method. The appendix contains proof of a few key results.

2 THE ABS METHOD

The ABS method is motivated by the analytical solution of \mathcal{D}_B derived under the ideal case of no instrument noise (§2.1). It is then extended to the case with instrument noise (§2.2).

2.1 The analytical solution for the case of no instrument noise

Our method works on $\mathcal{D}_{ij}(\ell)$, the $N_f \times N_f$ matrix of cross bandpower between the i -th and j -th frequency band. Here ℓ denotes the multipole bin. $i, j = 1, 2 \dots N_f$ and N_f is the total number of frequency bands. In thermodynamic units,

$$\mathcal{D}_{ij}(\ell) = f_i^B f_j^B \mathcal{D}_B(\ell) + \mathcal{D}_{ij}^{\text{fore}}(\ell). \quad (1)$$

Since we use the thermodynamic units, $f^B = 1$. $\mathcal{D}_{ij}^{\text{fore}}$ is the cross bandpower matrix of foreground. It has order N_f , but its rank M depends on the number of independent foreground components. Our task is to solve Eq. 1 for $\mathcal{D}_B(\ell)$, without assumptions of $\mathcal{D}_{ij}^{\text{fore}}$. This may appear as a mission impossible. However, due to the fact that CMB has a blackbody spectrum, and the fact that there may be limited foreground components in frequency space, Eq. 1 may be indeed solvable. We are able to prove the following two key results.

- **The solution to \mathcal{D}_B is unique, as long as $M < N_f$.** The proof is given in the appendix. A heuristic explanation is as follows. The matrix \mathcal{D}_{ij} has rank $M + 1$. Subtracting $\mathcal{D}_B f_i^B f_j^B$, the new matrix $\mathcal{D}_{ij} - \mathcal{D}_B f_i^B f_j^B$ will have rank M . Such reduction of 1 in rank happens and only happens when the trial value of \mathcal{D}_B exactly equals to its true value. This explains the existence and uniqueness of the solution \mathcal{D}_B .

- **The analytical solution exists, given by**

$$\mathcal{D}_B = \left(\sum_{\mu=1}^{M+1} G_\mu^2 \lambda_\mu^{-1} \right)^{-1}. \quad (2)$$

Here the μ -th eigenmode has eigenvector $\mathbf{E}^{(\mu)}$ and eigenvalue λ_μ . We adopt the normalization $\mathbf{E}^{(\mu)} \cdot \mathbf{E}^{(\mu)} = 1$. $G_\mu \equiv \mathbf{f}^B \cdot \mathbf{E}^{(\mu)}$. We rank the eigenmodes with decreasing order in λ_μ . Since \mathcal{D}_{ij} is positive definite, $\lambda_\mu > 0$. The derivation of Eq. 2 is given in the appendix.

Eq. 2 is not straightforward to understand. However, for the limiting case of $M \leq 2$, one can solve for all eigenmodes analytically and verify Eq. 2 by brute-force. This equation also confirms our intuition that foreground components orthogonal to the CMB signal in the frequency space should not interfere CMB reconstruction.

Eq. 2 is not the only analytical expression for \mathcal{D}_B . A set of expression is as follows,

$$\mathcal{D}_B = \left(\sum_{\mu=1}^{M+1} G_\mu^2 \lambda_\mu^{-1} \right)^{-1}_{\mathcal{D}_{ij} + \mathcal{S} f_i^B f_j^B} - \mathcal{S}. \quad (3)$$

The shift parameter \mathcal{S} is a free parameter. It shifts the input value of CMB signal from \mathcal{D}_B to $\mathcal{D}_B + \mathcal{S}$. G_μ and λ_μ are defined with respect to the new matrix $\mathcal{D}_{ij} + \mathcal{S} f_i^B f_j^B$. Eq. 2 is a special case of Eq. 3 with $\mathcal{S} = 0$. If there are no instrument noises nor numerical errors, Eq. 2 & 3 are equivalent. However, in reality Eq. 3 with positive \mathcal{S} is more stable, more accurate and therefore more useful for the B-mode determination.

2.2 Extension to the case with instrument noise

The ensemble average of the instrument noise on the diagonal elements can be subtracted. What remain in the matrix are random noises $\delta \mathcal{D}_{ij}^{\text{inst}}$,

$$\mathcal{D}_{ij}^{\text{obs}} \equiv \mathcal{D}_{ij} + \delta \mathcal{D}_{ij}^{\text{inst}}. \quad (4)$$

The residual noise has zero mean ($\langle \delta \mathcal{D}_{ij}^{\text{inst}} \rangle = 0$). Different noise matrix elements are uncorrelated. The associated dispersion in each noise matrix element is $\langle (\delta \mathcal{D}_{ij}^{\text{inst}})^2 \rangle = \sigma_{\mathcal{D},i}^{\text{inst}} \sigma_{\mathcal{D},j}^{\text{inst}} (1 + \delta_{ij})/2$. Eq. 2 & 3 can still be implemented in the data analysis, with some modifications to account for instrument noise.

Step 1. First we need to deal with the varying $\sigma_{\mathcal{D},i}^{\text{inst}}$ across frequency bands.¹ In this case, we should not treat each $\mathcal{D}_{ij}^{\text{obs}}$ with equal weight. Instead, we should weigh $\mathcal{D}_{ij}^{\text{obs}}$ by $\sqrt{\sigma_{\mathcal{D},i}^{\text{inst}} \sigma_{\mathcal{D},j}^{\text{inst}}}$,

$$\mathcal{D}_{ij}^{\text{obs}} \rightarrow \tilde{\mathcal{D}}_{ij}^{\text{obs}} \equiv \frac{\mathcal{D}_{ij}^{\text{obs}}}{\sqrt{\sigma_{\mathcal{D},i}^{\text{inst}} \sigma_{\mathcal{D},j}^{\text{inst}}}}. \quad (5)$$

The ABS method applies to $\tilde{\mathcal{D}}_{ij}^{\text{obs}}$, with the following operations,

$$\begin{aligned} f_i^B &\rightarrow \tilde{f}_i^B \equiv \frac{f_i^B}{\sqrt{\sigma_{\mathcal{D},i}^{\text{inst}}}}, \\ G_\mu &\rightarrow \tilde{G}_\mu \equiv \tilde{\mathbf{f}}^B \cdot \tilde{\mathbf{E}}^\mu, \quad \lambda_\mu \rightarrow \tilde{\lambda}_\mu. \end{aligned} \quad (6)$$

Here $\tilde{\mathbf{E}}^\mu$ is the μ -th eigenvector of $\tilde{\mathcal{D}}_{ij}^{\text{obs}}$ and $\tilde{\lambda}_\mu$ is the eigenvalue. By such normalization, the noise matrix in $\tilde{\mathcal{D}}_{ij}^{\text{obs}}$ has

¹ Real surveys have other complexities. The appendix §B will show that the ABS method is still applicable with the presence of masks and frequency dependent beams.

dispersion of 1 in the diagonal elements and $1/\sqrt{2}$ in the off-diagonal elements.

Step 2. We also need to deal with unphysical eigenmodes induced by instrument noise. With the presence of instrument noise, the rank of $\tilde{\mathcal{D}}_{ij}^{\text{obs}}$ will be N_f . The eigenmodes of instrument noises have typical amplitude ~ 1 and their distribution is symmetric. Therefore we must exclude eigenmodes with negative eigenvalues. We should also exclude eigenmodes with small eigenvalues. We choose the threshold $\lambda_{\text{cut}} \sim 1$. We compute all N_f eigenmodes of $\tilde{\mathcal{D}}_{ij}^{\text{obs}}$, and then measure \mathcal{D}_B from Eq. 3, but only using eigenmodes with $\lambda_\mu > \lambda_{\text{cut}}$. Namely, the estimator of \mathcal{D}_B with the presence of instrument noise is

$$\hat{\mathcal{D}}_B = \left(\sum_{\lambda_\mu \geq \lambda_{\text{cut}}} \tilde{G}_\mu^2 \tilde{\lambda}_\mu^{-1} \right)^{-1} \tilde{\mathcal{D}}_{ij}^{\text{obs}} + S \times \tilde{f}_i^B \tilde{f}_j^B - S. \quad (7)$$

Step 3. In this step we carry out a convergence test/self-calibration procedure to determine a suitable choice of S and then use it to obtain \mathcal{D}_B . S changes the distribution of physical eigenmodes. Larger positive S makes the matrix operations more stable and the impact of instrument noise weaker. By increasing S and finding the converged value of $\hat{\mathcal{D}}_B$, we obtain a more reliable measure of \mathcal{D}_B . We emphasize two points. First, both S and \mathcal{D}_B are self-determined from the data and no extra uncertainties are introduced in this step. Second, this step is also necessary to pass the null test detailed later.

3 SIMULATED OBSERVATIONS FOR TESTS

Next we test the ABS method on simulated $\mathcal{D}_{ij}^{\text{obs}}$ with a variety of foregrounds, instrument noise and survey frequency configurations.

3.1 Foreground specifications

For foregrounds, we specify

$$\mathcal{D}_{ij}^{\text{fore}} = \sum_{\alpha=1}^M f_i^{(\alpha)} f_j^{(\alpha)} \mathcal{D}_\alpha. \quad (8)$$

$f_i^{(\alpha)} \equiv f^{(\alpha)}(\nu_i)$ is the frequency dependence of the α -th foreground component and \mathcal{D}_α is the bandpower amplitude. Throughout the paper, we include two polarized foregrounds (galactic dust and galactic synchrotron). When we consider decorrelation between galactic dust at different frequency, we need at least two $f^\alpha(\nu)$ to describe dust alone. Therefore $M = 2$ if no decorrelation and $M \geq 3$ when decorrelation exists.

We consider four foreground models (case A, B, C, D, Fig. 1). They all share the same synchrotron foreground, but different dust foregrounds. For synchrotron,

$$f^{\text{syn}}(\nu) \propto \nu^{-\beta_{\text{syn}}/2} \frac{(e^x - 1)^2}{e^x x^4}, \quad \mathcal{D}_{\text{syn}} \propto \ell^{-0.6}. \quad (9)$$

Here $\beta_{\text{syn}} = 3.3$ is the frequency index and $x \equiv h\nu/(k_B T_{\text{CMB}})$. The bandpower is normalized as $3 \times 10^{-4} \mu\text{K}^2$, at $\nu = 150$ GHz and $\ell = 80$. This is the observationally allowed upper limit in the BICEP2 sky (BICEP2/Keck and Planck Collaborations et al. 2015).

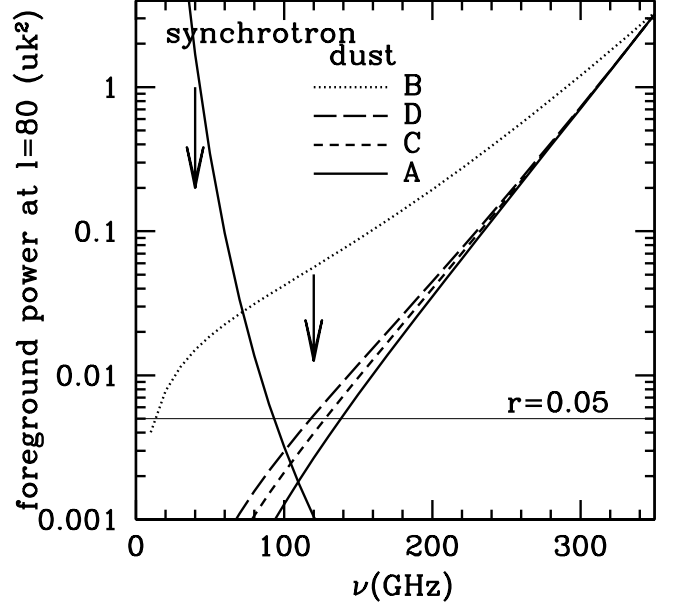


Figure 1. The foreground models for simulated observations to test the ABS method. The 4 models share identical synchrotron foreground, but different dust model parameters. Case C and D differ from case A and B by significant decorrelation between dust foregrounds at different frequencies. Case B and D have exaggerated dust contamination and are served to test the generality of our method.

For the galactic dust foreground, we adopt (Planck Collaboration et al. 2016b)

$$f^{\text{dust}}(\nu) \propto \frac{x^{\beta_d} (e^x - 1)^2}{x e^x (e^{x T_{\text{CMB}}/T_d} - 1)}, \quad \mathcal{D}_{\text{dust}} \propto \ell^{-0.42}. \quad (10)$$

To account for the recently detected decorrelation between different Planck frequency bands (Planck Collaboration et al. 2016a), we adopt a simple model of spatially stochastic variation in the dust index β_d (Planck Collaboration et al. 2016a). It induces a new component in $\mathcal{D}_{ij}(\ell)$,

$$f^S(\nu) = f^{\text{dust}}(\nu) \times \ln(\nu/\nu_0), \quad \mathcal{D}_S = \mathcal{D}_{\text{dust}} A_S. \quad (11)$$

Here we adopt $\nu_0 = 353$ GHz. $A_S \propto \langle \delta\beta_d^2 \rangle$ is a free parameter to control the level of decorrelation. When this stochastic component is subdominant, the cross correlation coefficient between dust in i -th and j -th bands is $\mathcal{R}_{\nu_i \nu_j}^{\text{BB}} \simeq 1 - \frac{1}{2} A_S (\ln(\nu_i/\nu_j))^2$. The overall bandpower is normalized as $3.5 \mu\text{K}^2$ at $\ell = 80$ and 353 GHz (BICEP2/Keck and Planck Collaborations et al. 2015).

We adopt 4 cases of dust parameters, $(\beta_d, T_d, A_S) = (1.59, 19.6, 0.0), (0.5, 10, 0.0), (1.59, 19.6, 0.42), (1.59, 19.6, 0.84)$. Case A is the best fit of Planck (Planck Collaboration et al. 2016b). Case B has a factor of 10 more dust contamination at 100-150 GHz than case A, and also a much flatter spectrum. Case C has dust decorrelation between frequency bands, reproducing the Planck finding of $\mathcal{R}_{353,217}^{\text{BB}} = 0.95$ (Planck Collaboration et al.

Table 1. We test our ABS method against various CMB frequency configurations and instrumental noise. σ_D^{inst} is the r.m.s. error in the bandpower measurement caused by instrumental noise.

Labels	frequency/GHz	$\sigma_D^{\text{inst}}/\mu\text{K}^2$
F0	30, 70, 100, 150, 217 & 353	
F1	95, 150, 220 & 270	
F2	35, 95, 150, 220 & 270	
F3	35, 95, 150, 220, 270 & 353	$(10^{-5}, 10^{-2})$
F4	30, 36, 43, 51, 62, 75, 90, 105, 135 160, 185, 200, 220, 265, 300 & 320	

2016a). Case D has unrealistically large decorrelation (e.g. $\mathcal{R}_{353,150}^{BB} = 0.7$).

3.2 Frequency configurations

Frequency configuration is crucial for foreground removal. We consider five configurations (**F0-F4**), shown in Table 1.

- **F0** is the fiducial one, with 6 bands centered at 30, 70, 100, 150, 217 & 353 GHz. This configuration is similar to Planck. It has a wide frequency coverage, good for both synchrotron and dust foreground removal.
- **F1** has 4 bands at 95, 150, 220 & 270 GHz (Keck array-like, Grayson et al. (2016)). A major difference of **F1** to **F0** is the lack of low frequency bands and hence limited capability of synchrotron foreground identification and removal.
- **F2** adds a 35 GHz bands to **F1** (BICEP array-like, Grayson et al. (2016)). This is to test the gain adding a low frequency band.
- **F3** further adds a 353 GHz band to **F2**. This turns out to be important for dust foreground removal when decorrelation in dust foreground exists.
- **F4** has 16 bands between 30 GHz and 320 GHz. This is basically the frequency configuration of PRISM (André et al. 2014), expect that PRISM also has higher frequency bands. Other proposed space missions such as CORE, PIXIE and LiteBIRD have similar configurations.

3.3 B-mode signal and physical eigenmodes

For the CMB signal, we focus on $\ell = 80$ around the recombination bump. The fiducial $\mathcal{D}_B = 5 \times 10^{-3} \mu\text{K}^2$, corresponding to the sum of $r = 0.05$ and the lensing B-mode. We also consider $\mathcal{D}_B = 2 \times 10^{-3} \mu\text{K}^2$ in which the lensing B-mode dominates. We further test around $\ell = 5$ of the reionization bump, with the choices of $\mathcal{D}_B = 1, 2 \times 10^{-3} \mu\text{K}^2$.

The eigenmodes of \mathcal{D}_{ij} depend on foregrounds, CMB signal and observational frequency configuration. Two useful relations to understand these eigenmodes are

$$\begin{aligned} \sum_{\alpha=1}^{M+1} \lambda_{\alpha} &= \text{Tr} \mathcal{D}_{ij} = \sum_{i=1}^{N_f} \mathcal{D}_{ii}, \\ \sum_{\alpha=1}^{M+1} \lambda_{\alpha}^2 &= \sum_{ij} \mathcal{D}_{ij}^2. \end{aligned} \quad (12)$$

Fig. 2 shows the eigenmodes for foreground model C, $\mathcal{D}_B = 5 \times 10^{-3} \mu\text{K}^2$, and frequency configuration **F0**. It has 4

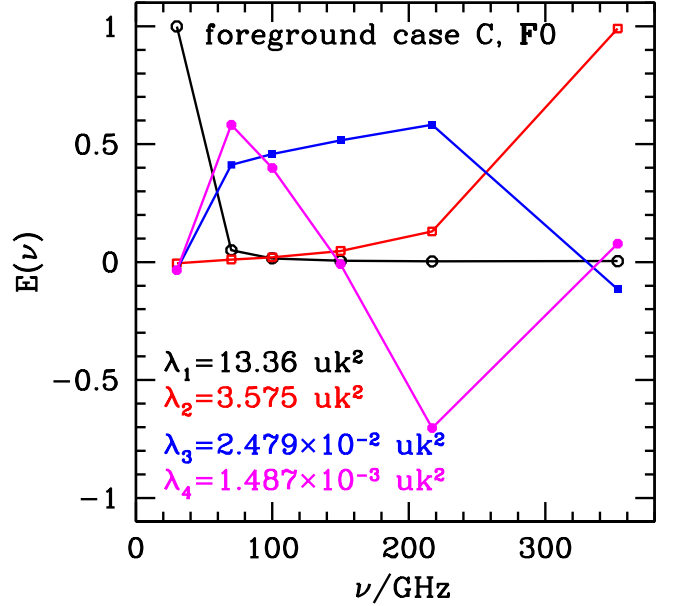


Figure 2. The eigenvectors and eigenvalues for foreground case C and frequency configuration **F0**, with $\mathcal{D}_B = 5 \times 10^{-3} \mu\text{K}^2$ and centered at $\ell = 80$. Due to significant decorrelation of thermal dust foreground, case C has 4 eigenmodes. (1) The first eigenmode (open circle) is dominated by synchrotron foreground, with eigenvalue λ_1 essentially its band power at 30 GHz. Since the synchrotron model is actually the observational upper limit, this eigenmode may be less significant in reality. (2) The second eigenmode (open square) is dominated by dust emission, with λ_2 essentially the dust emission band power at 353 GHz. (3) The third eigenmode (filled square) is dominated by CMB B-mode. (4) The fourth eigenmode (filled circle) is a mixture of all foreground and CMB components. Although it is subdominant, it is important for unbiased CMB measurement.

eigenmodes. The first two are essentially synchrotron and dust foreground, respectively. These can be seen from their frequency dependences (the shapes of eigenvectors). Furthermore, $\lambda_1 \simeq \sum_i \mathcal{D}_{ii}^{\text{syn}} \sim \mathcal{D}_{11}^{\text{syn}}$, $\lambda_2 \simeq \sum_i \mathcal{D}_{ii}^{\text{dust}} \sim \mathcal{D}_{66}^{\text{dust}}$. The third one is dominated by CMB, $\lambda_3 \simeq 5\mathcal{D}_B$. It is close to $N_f \mathcal{D}_B = 6\mathcal{D}_B$, the limit of pure CMB B-mode. For the same reason, it contains non-negligible contamination from foregrounds. The fourth eigenmode is a mixture of CMB and foregrounds, with a frequency dependence resembling none of CMB and foregrounds. This eigenmode is also important for CMB measurement, as will be shown later.

3.4 Instrument noise specifications

To generate simulated $\mathcal{D}_{ij}^{\text{obs}}$, we approximate $\delta \mathcal{D}_{ij}^{\text{inst}}$ as Gaussian random fields with dispersion $\sigma_{\mathcal{D},ij}^{\text{inst}}$. For brevity, we assume $\sigma_{\mathcal{D},11}^{\text{inst}} = \sigma_{\mathcal{D},22}^{\text{inst}} = \dots = \sigma_{\mathcal{D}}^{\text{inst}}$ ($i = 1, \dots, N_f$). Therefore $\mathcal{D}_{ij}^{\text{obs}}$ and $\tilde{\mathcal{D}}_{ij}^{\text{obs}}$ only differ by a uniform normalization. This allows us to work directly on $\mathcal{D}_{ij}^{\text{obs}}$, whose physical meaning is clearer than $\tilde{\mathcal{D}}_{ij}^{\text{obs}}$. Notice that the off-diagonal elements have smaller dispersion ($\sigma_{\mathcal{D}}^{\text{inst}}/\sqrt{2}$).

Reducing instrument noise is a key task in CMB po-

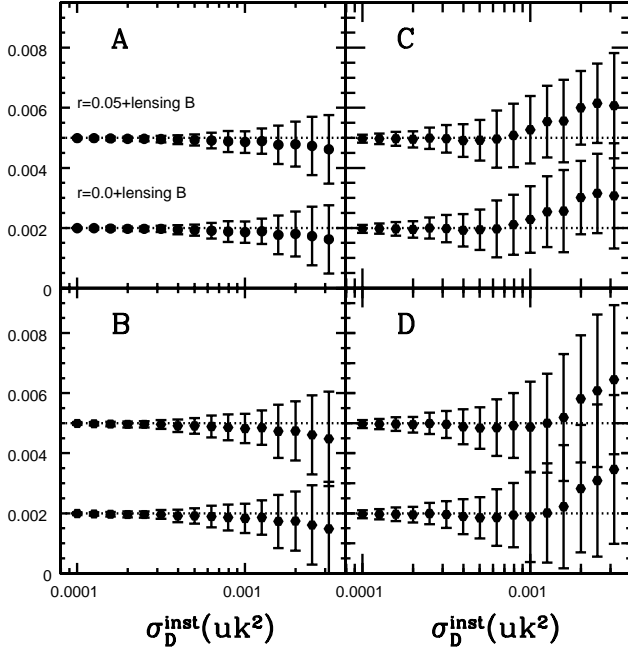


Figure 3. Tests for the F0 survey configuration and 4 cases of foregrounds. The y -axis is the bandpower in unit of μK^2 . Dot lines are the input B-mode. Points are the ABS output, as a function of bandpower measurement error $\sigma_{\mathcal{D}}^{\text{inst}}$. The error bars are estimated using 200 realizations of instrument noise. The input \mathcal{D}_{B} is recovered unbiasedly. We emphasize that the adopted foreground cases are to generate simulated observational data. Our ABS method assumes nothing about these foregrounds.

larization experiments. BICEP2/Keck has reached $\sigma_{\mathcal{D}}^{\text{inst}} \sim 10^{-3} \mu\text{K}^2$ (BICEP2/Keck and Planck Collaborations et al. 2015). Future experiments can go well below $10^{-4} \mu\text{K}^2$. For example, planned ground CMB-S4 projects (Abazajian et al. 2016) will have two orders of magnitude more detectors than BICEP2 ($\sim 5 \times 10^5$) and therefore a factor of 10 reduction in instrument noise. PRISM (André et al. 2014) has typical noise $\sim 70 \mu\text{K}/\text{detector}/\text{arcmin}^2$, ~ 200 detectors per band, $\sigma_{\mathcal{D}}^{\text{inst}} \simeq 3.7 \times 10^{-5} \mu\text{K}^2 (\ell/\Delta\ell)^{1/2} (0.5/f_{\text{sky}})^{1/2} (\ell/80)$. Here $\Delta\ell$ is the width of multipole bin and f_{sky} is the fractional sky coverage. Other experiments such as CORE (Delabrouille et al. 2017), EPIC and LiteBIRD have similar sensitivity. We consider a wide range of $\sigma_{\mathcal{D}}^{\text{inst}} \in (10^{-5}, 10^{-2}) \mu\text{K}^2$ to include all these possibilities.

4 TESTING THE ABS METHOD

Fig. 3 shows the test result for the F0 frequency configuration at $\ell \sim 80$. Throughout the paper, we fix the cut $\lambda_{\text{cut}} = 1/2$. Whether this choice of λ_{cut} is optimal and whether further improvement can be achieved are open questions for future investigation. The statistical error, for each noise level, foreground and signal, is estimated using 200 realizations of instrument noises (but identical CMB and foregrounds). For all investigated foregrounds, signal and noise

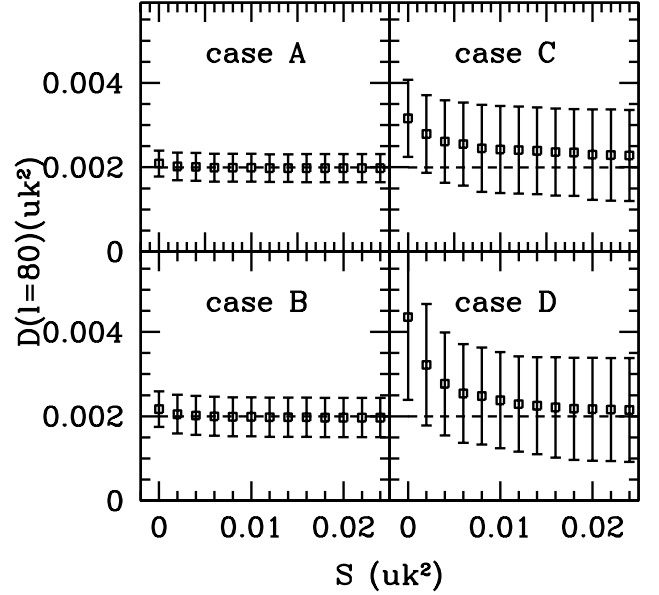


Figure 4. The convergence test and self-calibration process. We test the output \mathcal{D}_{B} as the function of \mathcal{S} , for $\mathcal{D}_{\text{B}} = 2 \times 10^{-3} \mu\text{K}^2$ and $\sigma_{\mathcal{D}}^{\text{inst}} = 10^{-3} \mu\text{K}^2$. By choosing sufficiently large \mathcal{S} , systematic error in the reconstruction can indeed be alleviated.

levels, our method faithfully extracts the input B-mode. It is unbiased even for high level of instrument noise $\sigma_{\mathcal{D}}^{\text{inst}} \sim \mathcal{D}_{\text{B}}$.

4.1 Convergence test and self-calibration

The above results are obtained adopting $\mathcal{S} = 20\sigma_{\mathcal{D}}^{\text{inst}}$. We emphasize that such value of \mathcal{S} is not chosen arbitrarily. It is self-determined by the data, through the step 3 of the ABS method (§2.2). The choice of \mathcal{S} is not important when $\sigma_{\mathcal{D}}^{\text{inst}} \ll \mathcal{D}_{\text{B}}$. However, it will become important when $\sigma_{\mathcal{D}}^{\text{inst}} \sim \mathcal{D}_{\text{B}}$. For $\mathcal{D}_{\text{B}} = 2 \times 10^{-3} \mu\text{K}^2$ and $\sigma_{\mathcal{D}}^{\text{inst}} = 10^{-3} \mu\text{K}^2$, Fig. 4 shows the ABS output adopting various shift parameter \mathcal{S} . For small value of \mathcal{S} systematic bias in \mathcal{D}_{B} can develop. At $\mathcal{S} = 0$, the systematic bias becomes greater than 1σ for case C and D (Fig. 4). But with increasing \mathcal{S} , this bias vanishes eventually and the estimated \mathcal{D}_{B} converges. Hereafter we adopt $\mathcal{S} = 20\sigma_{\mathcal{D}}^{\text{inst}}$. Fig. 3 shows that this choice of \mathcal{S} returns unbiased result for all other cases of foregrounds and \mathcal{D}_{B} .

4.2 Null test

We also carry out a null test of the ABS method by setting the input signal zero. The $\mathcal{S} = 0$ version of ABS (Eq. 7) fails the null test since it always returns positive value. Furthermore, the output result can be very unstable (e.g. leftmost data points of Fig. 5). Fortunately with $\mathcal{S} \sim 10\sigma_{\mathcal{D}}$ that can pass the convergence test, the null test is also passed. This again demonstrates that step 3 of the ABS method is necessary. We address here that the choice of \mathcal{S} does not induce extra uncertainty in the CMB measurement, because it is

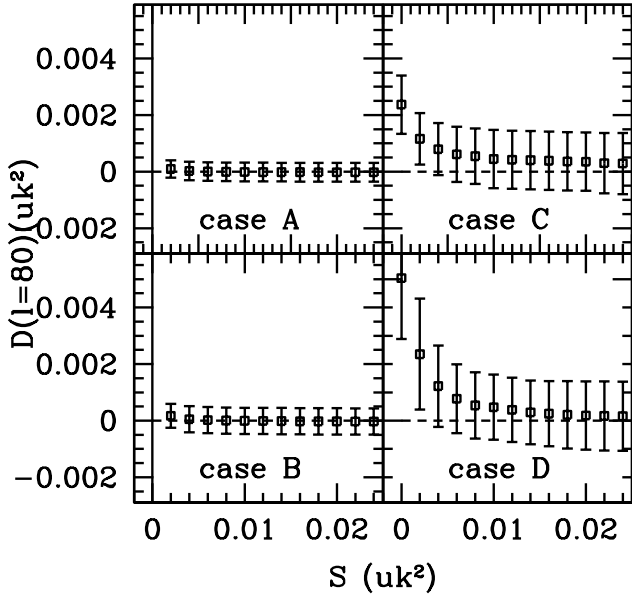


Figure 5. The null test result for the noise level $\sigma_D^{\text{inst}} = 10^{-3} \mu\text{K}^2$. We set the signal as zero and check the ABS output. The $S = 0$ version of the ABS method fails the null test since by design it always returns positive value. But S which passes the convergence test (Fig. 4) automatically passes the null test.

completely fixed by the data itself through the convergence test in §4.1.

4.3 Statistical errors

Fig. 6 plots the statistical error of the estimated \mathcal{D}_B as a function of instrument noise σ_D^{inst} . Roughly speaking, the statistical error $\sigma_B \propto \sigma_D^{\text{inst}}$. This is what we expect from our analytical prediction. Fig. 6 also compares σ_B with $\sigma_{\text{min}} \equiv \sigma_D^{\text{inst}} / \sqrt{N_f(N_f + 1)/2}$. The latter is a lower bound of statistical error. It corresponds to the limit of no foreground contaminations in which we can simply average over all cross correlation measurements. The presence of foreground enlarges the statistical error, by a factor of ~ 2 for case A/B and a factor of ~ 6 for case C/D.

4.4 Insensitivity to foregrounds

The above results also show that the recovery of B-mode by ABS is insensitive to the overall amplitude and spectral shape of galactic foregrounds. For example, case B has a factor of ~ 10 larger dust contamination at ~ 150 GHz band than case A. It also has a much flatter spectrum. Both would severely degrade the CMB extraction. However, the performance is almost as good as case A, without statistically significant bias. The only major difference is that the statistical error is about 40% larger (Fig. 6).

Furthermore, our ABS method also works when decorrelation of foregrounds at different frequencies exists (case

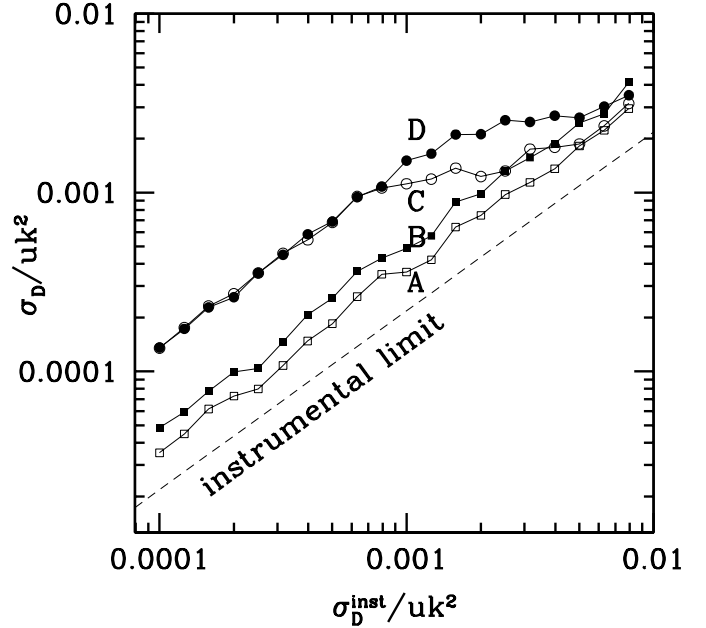


Figure 6. The dependence of the statistical error σ_D on the instrument bandpower error σ_D^{inst} per band. σ_D at $\ell \sim 80$ and survey configuration “F0” is shown for the foreground cases of A, B, C and D, respectively. The dash line is the instrumental limit $\sigma_D^{\text{inst}} / \sqrt{N_f(N_f + 1)/2}$ which can only be achieved when foregrounds are negligible.

C & D, Fig. 3). Case C & D have one more dust component, so one can not simply scale from high frequency maps to low frequency maps to remove dust foreground. Our method nevertheless recovers the input B-mode, robustly and blindly. This demonstrates the advantage that the ABS method needs no assumptions on the number of independent foreground components.

Fig. 7 shows the test results at $\ell \sim 5$ around the reionization bump (Fig. 7). Again the ABS successfully recovers the input B-mode. The signal, foregrounds and instrument noises at $\ell \sim 5$ are very different to that at $\ell \sim 80$. The synchrotron and dust foregrounds are a factor of 5 and 3 larger, respectively. The B-mode signal is dominated by primordial gravitational wave B-mode, with an amplitude $\lesssim 2 \times 10^{-3} \mu\text{K}^2$. Therefore the overall B-mode signal to foreground ratio is a factor of ~ 10 smaller than that at $\ell \sim 80$. Success of ABS for the $\ell \sim 5$ then further demonstrates its insensitivity to foreground properties.

5 SURVEY REQUIREMENTS FOR UNBIASED MEASUREMENT

The success of ABS against the variety of foreground models, CMB signal and instrument noise levels investigated above is encouraging. Nonetheless, certain survey requirements have to be satisfied to achieve unbiased CMB measurement. If a survey is lack of necessary frequency coverage or is lack of necessary sensitivity, it may fail to correctly identify one or more foreground components. If such foregrounds are not

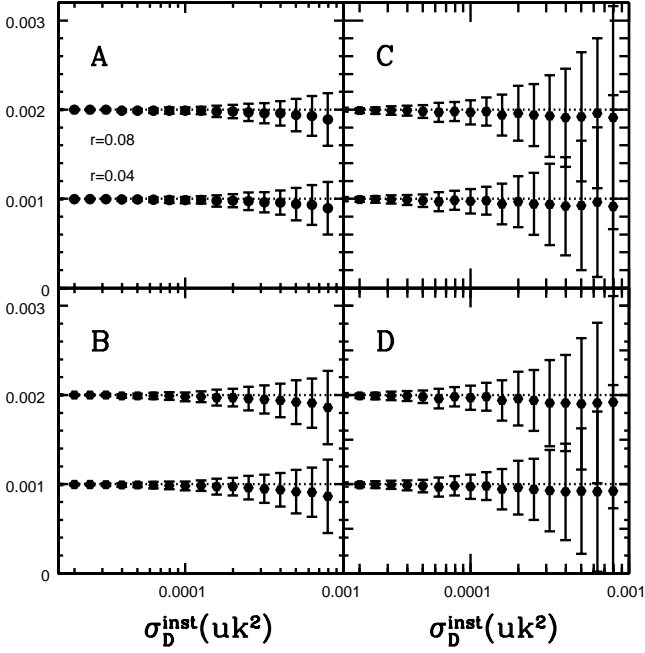


Figure 7. Similar to Fig. 3, but for $\ell = 5$ around the reionization bump. The y -axis is the bandpower in unit of μK^2 . Notice that, due to smaller B-mode at this scale and smaller instrumental noise (scales as ℓ^{-1}), we use different range of σ_D to that in Fig. 3.

orthogonal to CMB in frequency space, they will then lead to biased CMB estimation. The ABS method provides a specific diagnostic.

5.1 Bias induced by survey limitations

We demonstrate this point with the **F1-4** frequency configuration. It turns out that ABS still remains unbiased for model A and B, for all relevant noise levels. Therefore for brevity we only show the tests results for foreground case C (Fig. 8).

The foreground case C for testing has a large synchrotron component, together with two dust components. The **F1** frequency configuration only covers frequency $\gtrsim 90$ GHz and therefore has the poorest capability of separating the synchrotron component from others. Therefore should have the worst performance. The ABS output is unbiased only for very low instrumental noise ($\sigma_D^{\text{inst}} \lesssim 3 \times 10^{-5} \mu K^2$). Systematic bias quickly grows with increasing instrumental noise. When $\sigma_D^{\text{inst}} = 0.01 \mathcal{D}_B = 5 \times 10^{-5} \mu K^2$, the bias is already 20% and the significance is 1σ (foreground model C). The bias quickly increases to 40% when $\sigma_D^{\text{inst}} = 10^{-3} \mu K^2$, and becomes statistically significant (2.5σ). The fractional bias remains roughly a constant for larger σ_D^{inst} , but its significance becomes weaker due to increasing statistical error.

This bias decreases with decreasing synchrotron amplitude, but it can still be statistically significant even when the synchrotron is only 10% of the observational upper limit. It is therefore dangerous to neglect the possible synchrotron foreground. Adding more frequency channels can

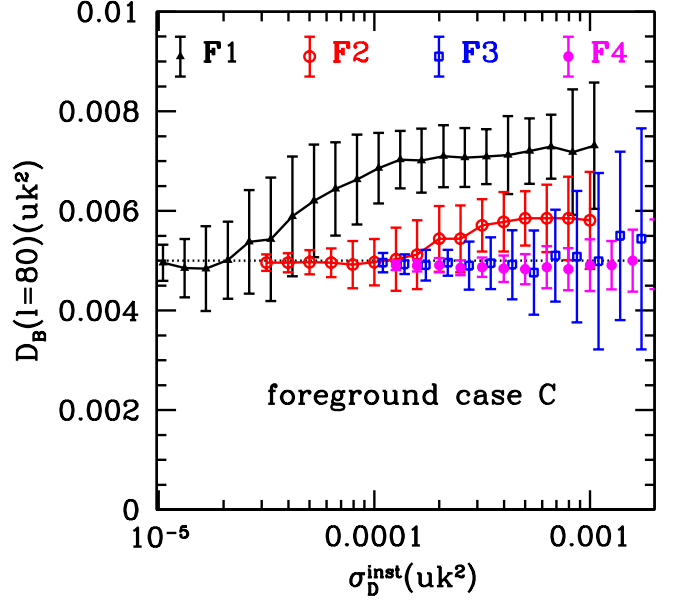


Figure 8. The impact of frequency coverage on CMB signal extraction. Incomplete frequency coverage (e.g. **F1**) and insufficient sensitivity cause failure in identifying certain eigenmodes significant for B-mode measurement (Fig. 9). This survey limitation causes bias in \mathcal{D}_B .

significantly improve the situation (Fig. 8). Adding a 35 GHz band (the **F2** configuration), the bias vanishes when $\sigma_D^{\text{inst}} \lesssim 3 \times 10^{-4} \mu K^2$. Further adding a 353 band (the **F3** configuration), the bias completely disappears and the performance of ABS is similar to the **F0** frequency configuration.

5.2 Survey requirements

The above tests show the following behaviors about the observed. (1) Incomplete frequency coverage alone may not necessarily lead to biased B-mode measurement, unless the instrumental noise exceeds certain threshold σ_D^{thres} . (2) The bias is positive, increases with σ_D^{inst} until reaching a plateau. These behaviors, along with the values of σ_D^{thres} and the bias, can be well understood within the framework of the ABS method. They actually reflect the limitation of a given CMB experiment.

We define

$$c_\alpha \equiv \frac{G_\alpha^2 / \lambda_\alpha}{\sum_{\mu=1}^{M+1} G_\mu^2 / \lambda_\mu}. \quad (13)$$

This is essentially the contribution of the α -th eigenmode to the measurement of $\mathcal{D}_B + \mathcal{S}$ (Eq. 2 & 3). If we miss this eigenmode, the ABS determined \mathcal{D}_B will be biased up by

$$\frac{\delta \mathcal{D}_B}{\mathcal{D}_B} = \frac{c_\alpha}{1 - c_\alpha} \times \left(1 + \frac{\mathcal{S}}{\mathcal{D}_B} \right) \equiv b_\alpha > 0. \quad (14)$$

The necessary condition of unbiased \mathcal{D}_B measurement by a given survey is that all eigenmodes of significant b_α

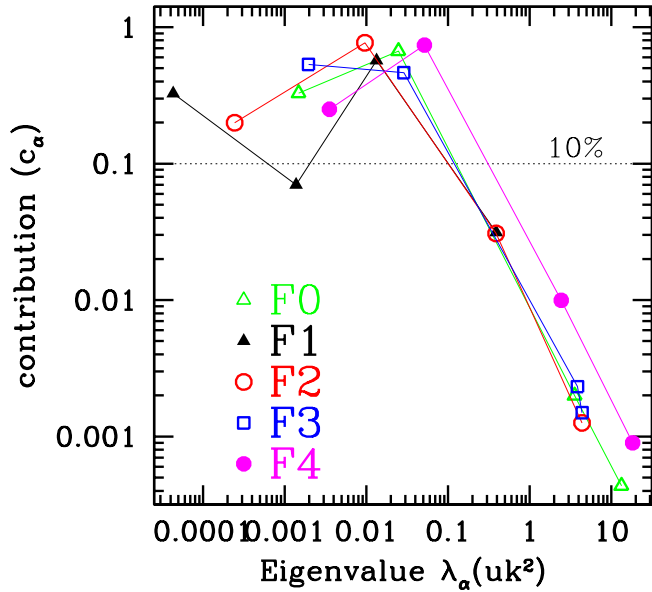


Figure 9. A diagnostic of unbiased B-mode extraction. The detection significance of the α -th eigenmode is $\lambda_\alpha/\sigma_{\mathcal{D}}^{\text{inst}}$. If $\lambda_\alpha \lesssim \sigma_{\mathcal{D}}^{\text{inst}}$, this eigenmode becomes in-detectable. This results in a fractional systematic error of $c_\alpha/(1 - c_\alpha)$ in \mathcal{D}_B . Incomplete frequency coverage leads to the existence of physical eigenmodes with small λ_α , but significant c_α .

must be robustly identified. The S/N of the α -th eigenmode is $\tilde{\lambda}_\alpha$. It is also the detection significance of this eigenmode. For our simplified case with identical instrument noise level across frequency bands, $\tilde{\lambda}_\alpha = \lambda_\alpha/\sigma_{\mathcal{D}}^{\text{inst}}$. Therefore, if $\lambda_\alpha \lesssim \sigma_{\mathcal{D}}^{\text{inst}}$, this eigenmode is overwhelmed by instrument noise and in-detectable. Inappropriate frequency coverage leads to the existence of such eigenmode with significant b_α but tiny λ_α . It then causes significant overestimation of \mathcal{D}_B .

Fig. 9 shows λ_α - c_α in the F0-F4 configurations for foreground case C. The CMB signal is $\mathcal{D}_B = 5 \times 10^{-3} \mu\text{K}^2$. The shift parameter $\mathcal{S} = 0$ so $c_\alpha = b_\alpha$. Fig. 10 shows the dependence of λ_α and c_α on the shift parameter \mathcal{S} . \mathcal{D}_{ij} of case C has $M + 1 = 4$ physical eigenmodes. The first two are usually dominated by foregrounds and therefore have large eigenvalues. But due to the $1/\lambda_\mu$ weighting in Eq. 2, their impacts on the B-mode extraction are automatically suppressed to a level negligible ($b_\alpha \ll 1$). Usually both the third and fourth eigenmodes have significant c_α , and therefore are important for B-mode extraction. The problem of F1 is that the fourth eigenmode has a large $c_4 = 0.33$ but a tiny $\lambda_4 = 4.3 \times 10^{-5} \mu\text{K}^2$. The operation of Eq. 7 with $\mathcal{S} > 0$ changes this eigenvalue, but b_4 is essentially unchanged (Fig. 10). Missing this eigenmode then biases \mathcal{D}_B up by $b_4 \simeq 50\%$. This explains the observed bias for the F1 frequency configuration, when $\sigma_{\mathcal{D}}^{\text{inst}} \gtrsim \lambda_4$ (Fig. 8).

Nevertheless, $\mathcal{S} > 0$ benefits the determination of CMB B-mode. The eigenvalue increases with increasing \mathcal{S} (Fig. 10). Therefore this eigenmode becomes more significant against instrument noise. For fixed instrument noise, it leads to reduced systematic error.

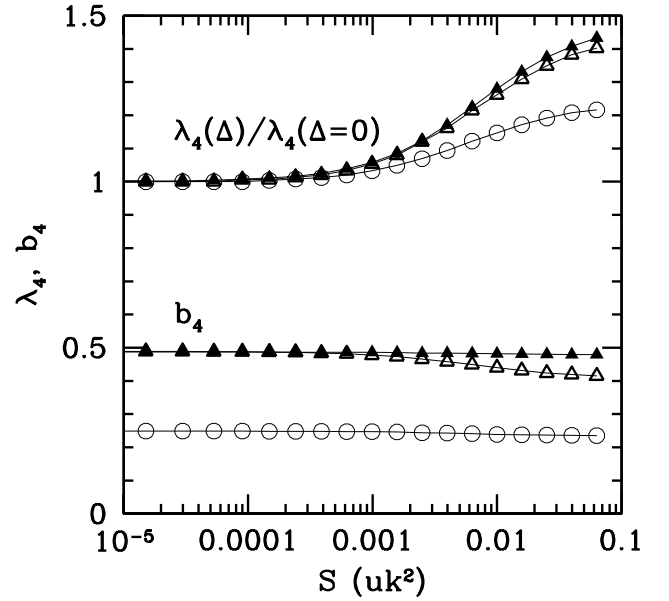


Figure 10. The dependence of the smallest eigenmodes on the shift parameter \mathcal{S} , for foreground model C and frequency configuration F0-3.

Adding the 35 GHz band (F2) improves the identification of synchrotron foreground. It leads to significantly larger $\lambda_4 = 2.4 \times 10^{-4} \mu\text{K}^2$ and significantly smaller $c_4 = 0.2$. This significantly improves the situation, until $\sigma_{\mathcal{D}}^{\text{inst}} \gtrsim \lambda_4$, where a bias of $b_4 \simeq 25\%$ develops. An extra 353 GHz band pushes all $\lambda_\alpha > 10^{-3} \mu\text{K}^2$ and the systematic error essentially vanishes.

Adding more frequency bands further reduces the risk of more complicated foregrounds. Future experiments such as CORE, PRISM and PIXIE will have dozens or more frequency bands, and low instrument noise ($\sigma_{\mathcal{D}}^{\text{inst}} \lesssim 10^{-4} \mu\text{K}^2$). Such high degree of redundancy would make them safe for even more complicated foregrounds. We expect them to achieve unbiased and precise measurement of \mathcal{D}_B (e.g. F4, Fig. 8).

Therefore Eq. 13 & 14 can be useful for survey design. Given the fiducial foreground and survey configurations, these equations tell us whether this survey is sufficient for B-mode detection, what survey depth is required, and what the gain of adding extra frequency channels is.

6 DISCUSSIONS AND CONCLUSIONS

The simulated data used for our tests includes both synchrotron and thermal dust foreground and takes decorrelation of dust foreground into account. However, it does not include other possible foregrounds such as spinning dust, due to large uncertainty in their understandings. In future works we plan to include more foregrounds, consider more realistic (and therefore more complicated) instrumental noise, and redo the tests carried out in this paper. Nevertheless, since our method makes no assumption on foreground, the success

of existing tests implies that it should also work with the existence of foregrounds other than synchrotron and thermal dust.

Our ABS method applies when survey windows/masks exist, as discussed in the appendix. We then conclude that our method is applicable to general case of foregrounds for blind, yet accurate, extraction of CMB B-mode. It is also numerically stable against various instrument noise. It further provides a quantitative requirement (Eq. 13) for unbiased B-mode measurement, useful for design of future CMB experiments.

The ABS method shares some similarities with the existing method SMICA and ILC, while has its own uniqueness. SMICA (spectral matching ICA) is a version of ICA (Delabrouille et al. 2003; Cardoso et al. 2008). Both SMICA and ABS work directly at the level of power spectrum, and solve essentially the same equations (Eq. 1). SMICA simultaneously fits many unknown parameters of CMB and foregrounds against the power spectrum measurements of all frequency bands and multipole bins. It has been successfully applied to the Planck data (e.g. Planck Collaboration et al. (2015b)). SMICA has the advantage of simultaneously solving for both CMB and foregrounds. It also has the advantage of fitting the instrument noise power spectrum, in case that one can not accurately calibrate/know the instrument noise from TOD data. ABS has the sole goal of solving for the CMB power spectrum, and therefore itself provides no information on foregrounds. The advantage is that it is based on the discovered analytical solution (Eq. 2), and computationally straightforward. Furthermore, ABS works on individual ℓ bin. It does not require assumptions on the scale dependence of foreground components (e.g. whether the foreground spectral dependence varies with ℓ). Therefore the two methods are highly complementary. For example, the two solutions of CMB solved by SMICA and ABS provide natural cross-checks to each other. The CMB solution provided by ABS can be used as CMB prior in SMICA to alleviate computational challenges in multiple parameter fitting. On the other hand, SMICA can identify foregrounds and provides useful information on the applicability of ABS, which requires $M < N_f$ to be unbiased. SMICA also provides a check whether we understand the instrument noise correctly and therefore if we subtract the noise ensemble average correctly in the ABS method.

The ILC method and various versions of it (e.g. Bennett et al. (2003); Tegmark et al. (2003); Eriksen et al. (2004); Basak & Delabrouille (2012, 2013)) are originally designed to minimize the variance in the reconstructed CMB map. Since foregrounds, in contrast to instrument noise, are fixed realizations of random processes, the reconstructed map is usually biased by residual foregrounds (Eriksen et al. 2004; Vio & Andreani 2008). Vio & Andreani (2008) proved that, when the number M of independent foregrounds (at map level) is smaller than the number N_f of frequency bands, and when instrument noise is negligible, the reconstructed map is unbiased. However, in realistic case with the presence of instrument noise, the ILC reconstructed CMB map is biased, even when the condition $M < N_f$ is satisfied. On the other hand, the ABS method is designed to achieve unbiased CMB power spectrum measurement, instead of minimizing variance. The analytical solution (Eq. 2) is derived directly from this specific goal. Un-

der the condition of no instrument noise and $M \leq N_f$, the ABS method is equivalent to the ILC method in harmonic space (Tegmark et al. 2003; Vio & Andreani 2008). In this case, ABS provides a proof of unbiased CMB reconstruction by ILC, independent of proofs in the literature (Vio & Andreani 2008). In realistic case where instrument noise exists, the two differ significantly. (1) The CMB power spectrum directly obtained from the ILC reconstructed map is $\mathcal{D}_B^{\text{ILC}} = 1/(\mathbf{f}_B(\mathcal{D}^{\text{obs}} + \mathbf{N})^{-1}\mathbf{f}_B^T)$. Here \mathcal{D}^{obs} is defined in Eq. 4. \mathbf{N} is the ensemble average of the noise matrix, which is diagonal and of full rank. This estimate of CMB power spectrum is biased and some de-biasing procedures are required to obtain unbiased power spectrum measurement (Saha et al. 2008; Dick et al. 2012). As a comparison, the CMB power spectrum obtained by the ABS method with the shift parameter $\mathcal{S} = 0$ is $\mathcal{D}_B^{\text{ABS}} = 1/(\mathbf{f}_B(\mathcal{D}^{\text{obs}})^{-1}_{\text{pseudo}}\mathbf{f}_B^T)$. The pseudo-inverse of \mathcal{D}^{obs} is defined by ignoring eigenmodes with eigenvalues smaller than $\lambda_{\text{cut}} \sim 1$. These eigenmodes are likely heavily contaminated by instrument noise and therefore should be excluded. It turns out that, this cut not only reduces systematic error, but also alleviates the amplification of statistical error. The difference between ABS and ILC increases with the noise-to-signal ratio of CMB experiment. It is significant for B-mode measurement, since for relevant CMB experiments the instrument noise is at least comparable to the elusive primordial B-mode signal. (2) The version of ABS that we recommend introduces a shift parameter $\mathcal{S} \sim 10\sigma_{\mathcal{D}}^{\text{inst}}$, which has no analogy in ILC. This non-zero \mathcal{S} is an essential ingredient in ABS. In particular, ABS with $\mathcal{S} \sim 10\sigma_{\mathcal{D}}^{\text{inst}}$ is able to pass the null test. Given that the lower bound of primordial B-mode amplitude is not constrained at all and given that the primary goal of ongoing B-mode experiments is to measure this amplitude, this null test is of crucial importance to demonstrate the robustness of B-mode detection. We then conclude that the ABS method is complementary to existing methods such as SMICA and ILC, and provide useful cross-checks. Nevertheless, the tests that we have carried out so far may still be too limited to fully explore the applicability of the ABS method. Furthermore, we have not tested it with real data, and therefore can not compare with sophisticated methods such as SMICA and ILC quantitatively. We leave these investigations for future study.

The ABS method works beyond the B-mode measurements. It also works for blind measurements of CMB temperature, E-mode polarization, the thermal SZ effect and CMB spectra distortion. Tests against simulated Planck maps has validated its applicability to simulated CMB temperature measurements (Yao et al. 2018). Furthermore, the ABS method has important applications even in totally different areas. For example, it may serve as the ultimate solution to the original proposal of extracting cosmic magnification by counting galaxies (Zhang & Pen 2005; Yang & Zhang 2011; Yang et al. 2015). An unresolved problem here is the stochasticity bias, which is analogous to multiple CMB foregrounds or decorrelation within each foreground component (e.g. thermal dust). The ABS method solves this problem, and is capable of reconstructing weak lensing to high accuracy (Yang et al. 2017; Zhang et al. 2018). Therefore we expect the ABS method to be promising and be useful in a variety of situations, and other potential applications should be explored as well.

7 ACKNOWLEDGMENTS

We thank Xuelei Chen, Xinjuan Yang and Yu Yu for useful discussions. We thank an anonymous referee for highly valuable suggestions. This work was supported by the National Science Foundation of China (11653003, 11433001, 11621303, 11320101002) and National Basic Research Program of China (2015CB857001, 2013CB834900).

REFERENCES

- Abazajian K. N., et al., 2016, preprint, ([arXiv:1610.02743](#))
 André P., et al., 2014, *J. Cosmology Astropart. Phys.*, **2**, 006
 BICEP2 Collaboration Ade P. A. R., et al. 2014, *Physical Review Letters*, **112**, 241101
 BICEP2/Keck and Planck Collaborations et al., 2015, *Physical Review Letters*, **114**, 101301
 Basak S., Delabrouille J., 2012, *MNRAS*, **419**, 1163
 Basak S., Delabrouille J., 2013, *MNRAS*, **435**, 18
 Bennett C. L., et al., 2003, *ApJS*, **148**, 97
 Bock J., et al., 2008, preprint, ([arXiv:0805.4207](#))
 Cardoso J.-F., Le Jeune M., Delabrouille J., Betoule M., Patanchon G., 2008, *IEEE Journal of Selected Topics in Signal Processing*, **2**, 735
 Delabrouille J., Cardoso J. ., 2007, ArXiv Astrophysics e-prints, Delabrouille J., Cardoso J.-F., Patanchon G., 2003, *MNRAS*, **346**, 1089
 Delabrouille J., et al., 2017, preprint, ([arXiv:1706.04516](#))
 Dick J., Castex G., Delabrouille J., 2012, preprint, ([arXiv:1203.4837](#))
 Draine B. T., Hensley B., 2012, *ApJ*, **757**, 103
 Eriksen H. K., Banday A. J., Górski K. M., Lilje P. B., 2004, *ApJ*, **612**, 633
 Gandilo N. N., et al., 2016, preprint, ([arXiv:1607.06172](#))
 Grayson J. A., et al., 2016, preprint, ([arXiv:1607.04668](#))
 Hivon E., Górski K. M., Netterfield C. B., Crill B. P., Prunet S., Hansen F., 2002, *ApJ*, **567**, 2
 Inoue Y., et al., 2016, in Millimeter, Submillimeter, and Far-Infrared Detectors and Instrumentation for Astronomy VIII. p. 99141I ([arXiv:1608.03025](#)), doi:10.1117/12.2231961
 Kamionkowski M., Kosowsky A., Stebbins A., 1997, *Physical Review Letters*, **78**, 2058
 Keisler R., Hoover S., Harrington N., Henning J. W., Ade P. A. R., Aird K. A., et al. 2015, *ApJ*, **807**, 151
 Kogut A., et al., 2011, *J. Cosmology Astropart. Phys.*, **7**, 025
 Li H., et al., 2017, preprint, ([arXiv:1710.03047](#))
 Matsumura T., et al., 2014, *Journal of Low Temperature Physics*, **176**, 733
 Planck Collaboration et al., 2011, *A&A*, **536**, A20
 Planck Collaboration et al., 2015b, preprint, ([arXiv:1502.05956](#))
 Planck Collaboration et al., 2015a, preprint, ([arXiv:1502.01588](#))
 Planck Collaboration et al., 2015c, preprint, ([arXiv:1506.06660](#))
 Planck Collaboration et al., 2015d, *A&A*, **576**, A107
 Planck Collaboration et al., 2016a, preprint, ([arXiv:1606.07335](#))
 Planck Collaboration et al., 2016b, *A&A*, **586**, A133
 Planck Collaboration et al., 2018, preprint, ([arXiv:1807.06208](#))
 Poh J., Dodelson S., 2016, preprint, ([arXiv:1606.08922](#))
 Remazeilles M., Dickinson C., Eriksen H. K. K., Wehus I. K., 2016, *MNRAS*, **458**, 2032
 Saha R., Prunet S., Jain P., Souradeep T., 2008, *Phys. Rev. D*, **78**, 023003
 Seljak U., 1997, *ApJ*, **482**, 6
 Seljak U., Zaldarriaga M., 1997, *Physical Review Letters*, **78**, 2054
 Starobinskiĭ A. A., 1979, Soviet Journal of Experimental and Theoretical Physics Letters, **30**, 682

- Tegmark M., de Oliveira-Costa A., Hamilton A. J., 2003, *Phys. Rev. D*, **68**, 123523
 Thornton R. J., et al., 2016, preprint, ([arXiv:1605.06569](#))
 Umiltà C., Cardoso J. F., Benabed K., Le Jeune M., 2018, preprint, ([arXiv:1807.00830](#))
 Vio R., Andreani P., 2008, *A&A*, **487**, 775
 Yang X., Zhang P., 2011, *MNRAS*, **415**, 3485
 Yang X., Zhang P., Zhang J., Yu Y., 2015, *MNRAS*, **447**, 345
 Yang X., Zhang J., Yu Y., Zhang P., 2017, *ApJ*, **845**, 174
 Yao J., Zhang L., Zhao Y., Zhang P., Santos L., Zhang J., 2018, preprint, ([arXiv:1807.07016](#))
 Zhang P., Pen U.-L., 2005, *Physical Review Letters*, **95**, 241302
 Zhang P., Yang X., Zhang J., Yu Y., 2018, preprint, ([arXiv:1807.00443](#))

APPENDIX A: THE DERIVATION OF THE ABS METHOD

A1 Uniqueness of solution

We first define vectors in frequency space of N_f dimensions, $\mathbf{f}^{(\alpha)} \equiv (f_1^{(\alpha)}, \dots, f_{N_f}^{(\alpha)})$. Without loss of generality, we absorb \mathcal{D}_α into corresponding $\mathbf{f}^{(\alpha)}$. Suppose that $(\sigma, \mathbf{h}^{(1)}, \dots, \mathbf{h}^{(M)})$ is also a set of solution to Eq. 1 & 8,

$$\mathcal{D}_{ij} = f_i^B f_j^B \sigma + \sum_{\beta=1}^M h_i^{(\beta)} h_j^{(\beta)}. \quad (\text{A1})$$

Then, $\mathbf{h}^{(\beta)}$ must be linear combinations of the eigenvector \mathbf{E}_s . Since \mathbf{E}_s are linear combinations of vector $\mathbf{f}^{(\alpha)}$ and \mathbf{f}^B , $\mathbf{h}^{(\beta)}$ must be linear combinations of $\mathbf{f}^{(\alpha)}$ and \mathbf{f}^B ,

$$\mathbf{h}^{(\beta)} = \left[\sum_{\alpha=1}^M R_{\alpha\beta} \mathbf{f}^{(\alpha)} \right] + B_\beta \mathbf{f}^B. \quad (\text{A2})$$

Here, $R_{\alpha\beta}$ and B_β are constants to be determined. Plug the above relation into Eq. A1 and compare with Eq. 1 & 8, we obtain

$$\sum_{\beta} R_{\alpha\beta} R_{\gamma\beta} = \delta_{\alpha\gamma}, \quad \sum_{\beta} R_{\alpha\beta} B_\beta = 0, \quad \mathcal{D}_B - \sum_{\beta} B_\beta^2 = \sigma. \quad (\text{A3})$$

The first relation state that the matrix \mathbf{R} is orthogonal, $\mathbf{R}^T \mathbf{R} = \mathbf{I}$ where \mathbf{I} is the unity matrix. Hence $\det \mathbf{R} = \pm 1$. Therefore

$$\det \mathbf{R} \neq 0 \text{ \& } \mathbf{R} \cdot \mathbf{B} = 0 \Rightarrow \mathbf{B} = 0 \Rightarrow \sigma = \mathcal{D}_B. \quad (\text{A4})$$

We then prove that the solution to \mathcal{D}_B is unique.

In contrast, solutions to $\mathbf{f}^{(\alpha)}$ are not unique, subject to transformation defined by \mathbf{R} with $\det \mathbf{R} = \pm 1$. Actually when $\det \mathbf{R} = 1$, \mathbf{R} is the unitary rotation matrix operating in the M dimension frequency space. It is only after we fix the physics of each fs, may we uniquely solve them.

A2 Analytical Solution of \mathcal{D}_B

From Eq. 1, we obtain $E_{\mu\nu} = G_\mu G_\nu \mathcal{D}_B + F_{\mu\nu}$. Here, $F_{\mu\nu} \equiv \sum_{ij} E_i^{(\mu)} \mathcal{D}_{ij}^{\text{fore}} E_j^{(\nu)}$ and $G_\mu \equiv \sum_i f_i^B E_i^{(\mu)}$. $E_{\mu\nu}$ is diagonal ($E_{\mu\nu} = \lambda_\mu \delta_{\mu\nu}$), with order $M+1$ and rank $M+1$. Moving $G_\mu G_\nu \mathcal{D}_B$ to the l.h.s., we obtain

$$E_{\mu\nu} - G_\mu G_\nu \mathcal{D}_B = F_{\mu\nu}. \quad (\text{A5})$$

The rank of \mathbf{F} is M , smaller than its order $M + 1$. As a result,

$$\det(E_{\mu\nu} - G_\mu G_\nu \mathcal{D}_B) = 0. \quad (\text{A6})$$

The Sylvester's determinant theorem states that for matrices \mathbf{A} ($m \times n$), \mathbf{B} ($n \times m$), \mathbf{X} ($m \times m$) and unitary matrix \mathbf{I}_n ($n \times n$),

$$\det(\mathbf{X} + \mathbf{AB}) = \det(\mathbf{X})\det(\mathbf{I}_n + \mathbf{BX}^{-1}\mathbf{A}). \quad (\text{A7})$$

Eq. A6 then becomes

$$0 = \det(\mathbf{E} - \mathbf{GG}^T \mathcal{D}_B) = \det(\mathbf{E})(1 - \mathcal{D}_B \mathbf{G}^T \mathbf{E}^{-1} \mathbf{G}).$$

Since $\det(\mathbf{E}) \neq 0$, we prove Eq. 2. It also proves the uniqueness of the solution for \mathcal{D}_B from Eq. 1.

A3 The error estimation

The measured band powers are subject to instrumental noise. After subtracting the ensemble average from the diagonal elements, there will still be random noise $\delta\mathcal{D}_{ij}^{\text{inst}}$ (with $\langle \delta\mathcal{D}_{ij}^{\text{inst}} \rangle = 0$) on top of \mathcal{D}_{ij} of Eq. 1. In the limit of small perturbations,

$$\delta\lambda_\mu = \delta\mathcal{D}_{\mu\mu}, \quad \delta\mathbf{E}^{(\mu)} = \sum_{\nu \neq \mu} \frac{\delta\mathcal{D}_{\mu\nu}}{\lambda_\mu - \lambda_\nu} \mathbf{E}^{(\nu)}. \quad (\text{A8})$$

Here $\delta\mathcal{D}_{\mu\nu} \equiv \sum_{ij} E_i^{(\mu)} \delta\mathcal{D}_{ij}^{\text{inst}} E_j^{(\nu)}$. Correspondingly,

$$\delta G_\mu = \sum_{\nu \neq \mu} \frac{\delta\mathcal{D}_{\mu\nu}}{\lambda_\mu - \lambda_\nu} G_\nu, \quad \delta E_{\mu\nu} = \delta\lambda_\mu \delta_{\mu\nu}.$$

Here we have required the eigenvectors to be normalized to unity, and for that, $E_{\mu\nu} = \lambda_\mu \delta_{\mu\nu}$. We obtain by perturbing Eq. 2,

$$\begin{aligned} \frac{\delta\mathcal{D}_B}{\mathcal{D}_B^2} &= - \sum_{\mu} (2\delta G_\mu \lambda_\mu^{-1} G_\mu - \lambda_\mu^{-2} \delta\lambda_\mu G_\mu^2) \\ &= - \sum_{\mu} \sum_{\nu \neq \mu} \frac{2\delta\mathcal{D}_{\mu\nu} G_\mu G_\nu}{(\lambda_\mu - \lambda_\nu) \lambda_\mu} + \sum_{\mu} \lambda_\mu^{-2} \delta\mathcal{D}_{\mu\mu} G_\mu^2. \end{aligned} \quad (\text{A9})$$

We now symmetrize the first term on the right side of the above equation. We can switch between $\mu \leftrightarrow \nu$ and take the average,

$$\begin{aligned} \frac{1}{2} \left(- \sum_{\mu} \sum_{\nu \neq \mu} \frac{2\delta\mathcal{D}_{\mu\nu} G_\mu G_\nu}{(\lambda_\mu - \lambda_\nu) \lambda_\mu} - \sum_{\nu} \sum_{\mu \neq \nu} \frac{2\delta\mathcal{D}_{\mu\nu} G_\mu G_\nu}{(\lambda_\nu - \lambda_\mu) \lambda_\nu} \right) \\ = \sum_{\mu, \nu \neq \mu} \frac{\delta\mathcal{D}_{\mu\nu} G_\mu G_\nu}{\lambda_\mu \lambda_\nu}. \end{aligned} \quad (\text{A10})$$

Therefore

$$\frac{\delta\mathcal{D}_B}{\mathcal{D}_B^2} = \sum_{\mu, \nu} \frac{\delta\mathcal{D}_{\mu\nu} G_\mu G_\nu}{\lambda_\mu \lambda_\nu}. \quad (\text{A11})$$

Notice that now the sum includes $\mu = \nu$ pairs. $\sigma_D^2 \equiv \langle \delta\mathcal{D}_B^2 \rangle$ can be derived using the following relation,

$$\begin{aligned} \langle \delta\mathcal{D}_{\mu\nu} \delta\mathcal{D}_{\rho\sigma} \rangle &= \sum_{ijklm} E_i^{(\mu)} E_j^{(\nu)} E_k^{(\rho)} E_l^{(\sigma)} \langle \delta\mathcal{D}_{ij} \delta\mathcal{D}_{kl} \rangle \\ &= \frac{1}{2} \sum_{ij} E_i^{(\mu)} E_j^{(\nu)} \sigma_{\mathcal{D},i}^{\text{inst}} \sigma_{\mathcal{D},j}^{\text{inst}} (E_i^{(\rho)} E_j^{(\sigma)} + E_i^{(\sigma)} E_j^{(\rho)}). \end{aligned} \quad (\text{A12})$$

The last expression uses the relation $\langle \delta\mathcal{D}_{ij} \delta\mathcal{D}_{km} \rangle = \sigma_{\mathcal{D},i}^{\text{inst}} \sigma_{\mathcal{D},j}^{\text{inst}} (\delta_{ik} \delta_{jm} + \delta_{im} \delta_{jk})/2$. The prefactor 1/2 ensures that

$\langle (\delta\mathcal{D}_{ii})^2 \rangle = (\sigma_{\mathcal{D},i}^{\text{inst}})^2$. For the simplified case $\sigma_{\mathcal{D},1}^{\text{inst}} = \sigma_{\mathcal{D},2}^{\text{inst}} = \dots = \sigma_{\mathcal{D}}^{\text{inst}}$, we have

$$\sigma_{\mathcal{D}} = \sigma_{\mathcal{D}}^{\text{inst}} \left(\sum_{\mu} \frac{G_\mu^2}{\lambda_\mu^2} \mathcal{D}_B^2 \right). \quad (\text{A13})$$

For general case of $\sigma_{\mathcal{D}}^{\text{inst}}$ varying with frequency, it is

$$\sigma_{\mathcal{D}} = \sum_{\mu} \frac{\tilde{G}_\mu^2}{\tilde{\lambda}_\mu^2} \mathcal{D}_B^2. \quad (\text{A14})$$

The above two results are for the case of $S = 0$. When $S \neq 0$, the factor \mathcal{D}_B shall be replaced by $\mathcal{D}_B + S$.

APPENDIX B: THE APPLICABILITY OF ABS IN REAL SURVEYS

The ABS method has been derived under simplified situations. So an immediate question is whether it can be applied to real CMB surveys. The main text incorporate the fact that different frequency bands have different instrument noises and therefore should have different weights to obtain optimal measurement of CMB B-mode. There are other complexities. The measured CMB is smoothed over the beam, which depends on frequency. The masks in general vary with frequency. Even if we adopt identical mask for all frequency bands, the interplay between beam and mask causes decorrelation of the CMB signal in different frequency bands. Here we outline a procedure to apply the ABS method with the presence of these complexities.

- **Step 1.** We smooth all maps to a fiducial beam $B^f(\theta)$, before masking. This beam should be identical for all frequency bands. It should be homogeneous and isotropic, for the convenience of later process. Therefore it should only depend on the angle θ between the pixel position (\hat{n}_{pixel}), and the sky position (\hat{n}) where the signal comes from. If the actual beams are also homogeneous, this step can be done efficiently in harmonic space by multiplying a_{lm} of the i -th frequency band by $B^f(l)/B_i(l, m)$. Here $B_i(l, m)$ is the beam of the i -th frequency band, which can be anisotropic. In reality, the beam is in general inhomogeneous (depending on \hat{n}_{pixel}) and this step shall be done pixel by pixel.

- **Step 2.** We chose and apply a common mask $M(\hat{n}_{\text{pixel}})$ for all frequency maps.

- **Step 3.** We then measure the cross band power between these smoothed/masked maps $\mathcal{D}_{ij}^{\text{S+M}}(\ell)$. We subtract the ensemble average of the instrument noise power spectra from the diagonal elements. We also estimate the r.m.s. of the residual instrument noise $\sigma_{\mathcal{D},i}^{\text{inst}}(\ell)$ in each map.

- **Step 4.** We then weigh $\mathcal{D}_{ij}^{\text{S+M}}$ by $\sqrt{\sigma_{\mathcal{D},i}^{\text{inst}} \sigma_{\mathcal{D},j}^{\text{inst}}}$ and obtain essentially the S/N matrix $\tilde{\mathcal{D}}_{ij}$. The ABS method then directly applies to

$$\tilde{\mathcal{D}}_{ij} \equiv \frac{\mathcal{D}_{ij}^{\text{S+M}}}{\sqrt{\sigma_{\mathcal{D},i}^{\text{inst}} \sigma_{\mathcal{D},j}^{\text{inst}}}} = \tilde{f}_i^B \tilde{f}_j^B \mathcal{D}_B^{\text{S+M}} + \tilde{\mathcal{D}}_{ij}^{\text{fore}}. \quad (\text{B1})$$

Here, $\tilde{f}_i^B \equiv f_i^B / \sqrt{\sigma_{\mathcal{D},i}^{\text{inst}}}$. $\mathcal{D}_B^{\text{S+M}}$ is the CMB band power, with beam $B^f(\theta)$ and mask M . The ABS method directly applies to the above equation and solves for $\mathcal{D}_B^{\text{S+M}}$.

- **Step 5.** It is then the standard procedure to deconvolve $\mathcal{D}_B^{\text{S+M}}$ for \mathcal{D}_B (e.g. Hivon et al. (2002)).

In particular, step 1 (smoothing) and step 2 (masking) are not interchangeable. Otherwise the CMB signal in different maps will not be linearly proportional to each other and the signal term in Eq. B1 does not have the form $\propto \tilde{f}_i^{\text{B}} \tilde{f}_j^{\text{B}}$.